Supplementary Materials for

Attention Renders Sensory Contents into Conscious State via Content-invariant Frontal-Posterior Coupling in Humans

Xilei Zhang, Yiru Lin, Zhuoren Jin, Kai Zhang, Wenjing Zhou, Sheng He, Yi Jiang, Chao Zhang, Liang Wang

Liang Wang: lwang@psych.ac.cn

Chao Zhang: zhangchao94306@163.com

The file includes:

Materials and Methods
Figs. S1 to S17
Table S1

Other Supplementary Materials for this manuscript include the following:

Movies S1 to S5

Materials and Methods

Participants

Forty-one healthy participants took part in Experiment 1. Among them, 21 (16 females, 24.19±2.54 years) participated the experiment reported in the main text. For two participants, their oral reports for probe trials were not correctly recorded due to technical issue. These two participants were thus excluded from analysis of oral reports but were included in the analyses of counting performance. To replicate the main findings, the other 20 participants (16 females, 23.1 ± 1.88 years) participated the follow-up replication experiment reported in the supplementary (see Fig.**S2**). This follow-up experiment was designed and performed using comparable sample size but recruiting a different experimenter and two new audio encoders (for more information see the section named 'Audio data collection and offline coding').

Twenty-one drug-resistant epilepsy patients (10 females, 24.48±6.91 years) participated in Experiment 2. Nineteen patients were from Tiantan Hospital, Capital Medical University, and two patients were from Yuquan Hospital, Tsinghua University. These patients underwent intracranial electrode implantation as part of their clinical evaluation for epilepsy surgery when noninvasive studies could not adequately localize the origin of their seizures. Among them, six patients did not have their pupil data recorded: the first four (S01-04) due to the eye tracker not being in place, and the other two (S16 and S17) due to poor eye signal quality, which prevented successful eye tracking. These six patients were excluded from pupil data analysis but were included in other analyses.

For both Experiment 1 and 2, all participants had normal or corrected-to-normal vision, had no history of head trauma or encephalitis, and provided written informed consent. The research protocol of Experiment 1 was approved by the review board at the Institute of Psychology, Chinese Academy of Sciences, and that of Experiment 2 was approved by the institutional review boards at the hospital sites.

Apparatus

The stimuli were presented using Psychophysics Toolbox (Brainard 1997, Pelli 1997) for MATLAB (The Mathworks, Natick, MA, USA) on a 21-inch gamma-corrected monitor with a resolution of 1920 × 1020 pixels and a refresh rate of 60 Hz. An infrared eye tracker system Eyelink Portable Duo (SR research, Kanata, Ontario, Canada) was used to monitor gaze location, saccade behavior and pupil size in both Exp1 and 2. Observers viewed the screen from about 60 cm away, using a chin rest to stabilize the head position in Exp1. The chin rest was not used in Exp 2, where, instead, epilepsy patients sitting in bed were told to minimize their head movement during the recording period (in remote recording mode).

Materials

Visual stimuli used consisted of central and peripheral streams. The central visual stream consisted of four numerical values (4, 5, 6, or 7) which were employed to create a rapidly alternating number sequence at a frequency of 10 Hz, presented within the central visual field.

The peripheral visual stream consisted of 48 visual stimuli, comprising 16 animal images, 16 object images, and 16 face images, and were presented at 4.0° visual eccentricity (Fig.**1a**). Additionally,

eight visual masks originally constructed using line segments and then created into different variants by rotating and flipping this original mask were included in the peripheral visual stream. A pair of nonmatching masks was randomly selected for each trial. The animal and object images, as well as the visual masks, were sourced from (Cohen, Ortego et al. 2020). The face images which are all emotionally neutral and differ in gender half by half, were initially obtained from (Ekman and Friesen 1975, Tottenham, Tanaka et al. 2009) and were then converted into simple line drawings using an open-source tool (http://jianbihua.renrensousuo.com/).

Both central and peripheral streams were created and controlled using Psychophysics Toolbox version 3 for MATLAB. All stimuli were presented on a white background (1920 × 1080 pixels, 60Hz monitor; thinkpad T490). Participants were seated 60cm from the monitor, thus making the average size of the line drawings 4.8° in side length, and the masks 6°.

Paradigm design and procedure

In the experiment, participants were instructed to fixate on a central cross while a central fast-alternating number stream and a peripheral visual stream were presented simultaneously and unfolding across time in each own pace. Participants maintained fixation on a small black fixation dot (0.5° in diameter) that was continuously visible throughout the procedure. Four demo videos of the stimulus presentation sequences are available in the Supplementary materials.

Central number sequence

For each trial, the central visual stream was a pseudo-randomly ordered temporal sequence of single number characters altering at 10 Hz. For number-counting blocks, the target number to be counted was chosen randomly and informed to the participant at the beginning of each block.

Peripheral visual stream consisting of masks and image

For each block of 72 trials, forty-eight images were divided into four groups (A, B, C, and D), each containing four animals, four objects, and four faces, with images from only one group used in any given block. Within a block, 24 visible_image trials (twice per image), 24 invisible_image trials (twice per image), 12 visible_blank trials and 12 invisible_blank trials were conducted in random order. All trials were conducted in mixed and random order. There was a 1000ms blank intertrial interval that occurred after each trial and before the next.

Visibility manipulation closely followed the methodology outlined in (Dehaene, Naccache et al. 2001, Cohen, Ortego et al. 2020). Visible trials in the peripheral stream comprised a ‘mask-blank-image-blank-mask’ sequence, with each mask and blank period lasting 200ms and 100ms, respectively, resulting in a total trial duration of 633ms. The image was surrounded by blanks, making it weakly masked and explicitly visible. In contrast, invisible trials followed a ‘blank-mask-image-mask-blank’ sequence, with the image closely surrounded by masks, rendering it heavily masked and thus invisible to observers. Both visible and invisible trials were followed by a 1000ms blank intertrial interval before the next trial.

For both visible and invisible trials, their blank control trials were set to mimic the mask and blank sequence, but replaced the middle image with a complete blank of the same duration (33ms). We

subtracted different measures of interest (see following) of blank control trials from that of invisible and visible image trials (exampled at Fig.**2a**), obtaining a clean mask-free measure tied to visibility state when the image was either invisible or visible, respectively.

General procedure of Exp1 and Exp2

Both Experiment 1 and Experiment 2 were conducted using a block design. In all trials and blocks, the central number stream was consistently presented alongside the peripheral image and mask stream. We manipulated attentional focus across different conditions: directing attention primarily to the central number stream (unattended blocks of Exp1 and Exp2), focusing mostly on the central number stream but also partially on the peripheral stream ('partially attended condition' of Exp1, achieved by randomly adding occasional probes, see following), or directing attention primarily to the peripheral stream ('attended condition' of Exp2).

In the unattended blocks of Experiment 1 (i.e., without probes, consisting of 2 blocks), participants were instructed to focus solely on counting while disregarding the peripheral stream. To achieve so, participants were not informed about probes, until after they finished unattended condition tasks. The peripheral stream was presented in either the left or right visual field, with the order determined randomly for each trial, but no more than three successive trials occurred at the same side.

In the partially attended blocks of Experiment 1 (i.e., with probe, 10 blocks), we still required participants to set high priority the counting task and perform at their best. The only difference was that this session shifted a bit of attention to peripheral image, by occasionally probing its visibility in 16.7% randomly selected trials (**Fig.1d**). In these trials, a probe cue, i.e., a square outlining the image (side length 4.8°), interrupted the trial sequence at two timepoints (0ms or 200ms after image offset). When seeing this probe, participants first pressed keys to complete counting as usual, to indicate how many target numbers they saw before probe. This was designed to hold the majority of attention towards counting, performing the counting task as best as possible while leaving only a small portion distracted to peripheral images. Otherwise, if too much attention was distracted to image, wo proposed too much attention supplied to image would lead to a saturation ceiling effect hindering us to detect to what extent consciousness might decay within a 200ms temporal gap (200ms versus 0ms). After the first key-press, color of the probe cue turned red, indicating the start of audio recording. Seeing this, participants were required to orally reported whether they saw the target image surrounded by masks. If yes, further reported its category and detailed identity. A typical report for probe within a visible_image trial was like 'I am sure I saw an animal image with a tail but I am not sure whether it was a cat or a dog'.

We set 12 probes per block (16.7%, out of 72 trials per block), with any two probes interleaved by 4~8 trials though participants were not informed of this rule. These probes appeared in 4 visible_image trials, 4 invisible_image trials, 2 visible_blank trials and another 2 invisible_blank trials. Half probes appeared at 0ms after image offset, half at 200ms after image offset. This 16.7% probe percentage enables reliable calculation of false alarm rates in blank trials (visible_blank and invisible_blank) and measurements of 200ms consciousness decay in image trials, while anchoring participants' attention to the central counting task to avoid attentional overflow to the periphery caused by excessive probes.

In Experiment 2 (block design), attention was directed to different streams randomly alternating block by block but with no more than two repetitions, to peripheral image in attended blocks but to central counting stream in unattended blocks. In attended blocks of Exp2, participants focused on an image categorization task, but neglecting the central number stream completely. To help stabilize attention to peripheral image, peripheral stream was displayed consistently in one visual field (either left or right) for all trials but randomly set across blocks. At the end of each trial, participant was provided a forced choice to class the peripheral critical image into either animal, object or face by pressing a corresponding key. In attended blocks, counting task was not performed any more. In unattended blocks of Exp2, same stimulus streams were presented on the screen and the only difference was that participants performed the central counting task instead. The image categorization task was not performed anymore and participants were required to totally ignore the peripheral stream.

Audio data collection and offline coding.

Audio data were collected for probe trials during the partially attended condition of Experiment 1. The laptop's built-in recording device was activated immediately after participants pressed the response key which indicated when they saw the target number. Then, participants orally reported whether they perceived the critical image (excluding masks) at the onset of the probe cue, if so, they identified the category and identity of the image. Audio data were recorded in real-time and later analyzed offline by two encoders. Importantly, both coders were blinded to the experimental conditions to ensure unbiased coding.

The audio data were coded into three dimensions. In the first dimension of visibility (i.e., whether the critical image was seen), scores of 0-3 corresponded to surely not seen, seemingly not seen, seemingly seen, and surely seen, respectively. In the dimensions of categorical and item-level accuracy (i.e., whether the reported category/item was correct), scores of 0-4 corresponded to surely wrong, likely wrong, neutrally not sure, likely correct, and surely correct, respectively. Between two coders, interrater reliability was high in all three dimensions (correlation coefficient close to 1, Fig.**S1a**).

Pupil data collection

During Experiment 1, participants rested their heads on a chin-rest to limit head movement. In Experiment 2, the chin-rest constraint was removed to increase comfort for epilepsy patients who were sitting in bed. However, participants in both experiments were instructed to minimize head movements during the recording period. In both experiments, eye-tracking data were acquired using the EyeLink Portable Duo SR Research eye-tracker with 1 ms temporal resolution (at 1000 Hz frequency) in remote head-free-to-move mode, recording data from the monocular eye with a higher signal-to-noise ratio. The camera-to-eye distance roughly fluctuated around 60 cm.

Pupil data preprocessing

The raw sampling data was preprocessed using the Matlab interface to Eyelink EDF files (https://osf.io/fxumn/, Version 1.0.1) provided by SR research to identify eye-tracking indices. Relevant eye-tracking events, such as fixations, blinks, and saccades, were detected for each

participant. This was achieved using the functions edfExtractInterestingEvents.m. The relevant variable values and timing information were then extracted using edfExtractVariables.m and edfExtractKeyEventsTiming.m, respectively.

For each participant, time series of eye-related variables (e.g., pupil gaze coordinates) were calculated independently for each combination of attention (attended versus unattended) and visibility (visible versus invisible, as well as corresponding blank control trials). This was based on epochs lasting from 500 ms before image onset to 1500 ms after image onset. Trials with missing values (typically caused by eye blinks) exceeding 25% of the timepoints were discarded from subsequent analysis.

iEEG: contact reconstruction and localization

Postoperative computed tomography (CT) images were coregistered to preoperative T1-weighted MR images using FreeSurfer (v6.0.0, http://surfer.nmr.mgh.harvard.edu/). The registration was visually verified and manually adjusted if necessary. The implanted electrodes and contacts were reconstructed using the stereotactic localization software (Qin, Tan et al. 2017).

Initially, the intracranial electroencephalography (iEEG) contacts were labeled with a cortical area based on Freesurfer's anatomical parcellation (Fischl, Salat et al. 2002) in native space. Subsequently, all converted iEEG contacts were further labeled in standard space using the Desikan-Killiany (DK) labeling protocol (Desikan, Ségonne et al. 2006), which is a widely used human cortical labeling protocol. During this process, the coordinates of all contacts were mapped onto a standard MNI space. Based on the MNI coordinates, contacts were further labeled to functional parcellations using atlases like the Human Connectome Atlas (Glasser, Coalson et al. 2016) and its extension (Huang, Rolls et al. 2022), as well as the Yeo 7 network (Yeo, Krienen et al. 2011), to evaluate their functional roles when necessary.

To distinguish gray matter (GM) contacts from white matter (WM) ones, a spherical region of interest (ROI) with a radius of 3.5 mm was first created for each contact around the electrode coordinate in native space and then transformed to the standard space. The percentage of voxels labeled as GM within the ROIs (inclusion) was calculated and compared to the percentage of voxels outside the ROIs (exclusion). If the probability of inclusion exceeded that of exclusion, the ROI was classified as GM; otherwise, it was categorized as WM or an unknown area. For each included ROI, the probability values were compared between brain areas involved, and the ROI contact was labeled as the structural area with the maximal probability value.

iEEG: data collection and preprocessing

For all 21 patients, intracranial electroencephalography (iEEG) data were recorded using a Nihon-Kohden recording system at a sampling rate of 2000 Hz. To ensure data quality and avoid potential confounds from interictal activity or seizures, we verified that no subclinical or clinical seizures occurred during or immediately before the experiment.

After acquisition, the iEEG data were analyzed using MATLAB combined with EEGLAB toolbox. The data were first bandpass-filtered from 0.5 to 200 Hz using a zero-phase delay finite impulse

response filter and then downsampled to 500 Hz. Noise at 50 Hz and its harmonics were removed using a notch filter. Subsequently, iEEG traces from each contact were visually inspected to identify and exclude bad channels and time segments containing artifacts such as epileptic activity, large-amplitude slow-wave drifts, or high-frequency activity. Importantly, this visual inspection was performed in a blinded manner to the experimental conditions. For each patient, the time series of all remaining valid contacts were re-referenced by subtracting the mean signal of all white matter (WM) contacts. This step aimed to remove globally shared background signals. This unbiased approach avoids introducing inter-contact variance due to the re-referencing procedure and enhances the replicability of the findings.

iEEG: ERP analysis

For event-related potential (ERP) analysis, preprocessed traces were first bandpass-filtered between 0.5 and 30 Hz before segmenting epochs. Since band filtering usually introduces edge artifacts at the head and tail of traces, this filtering step was crucial to ensure that data inter-between the head and tail (including all data of interest) were not contaminated by these artifacts. After filtering, the traces were segmented into epochs spanning from -500 ms before to 1000 ms after image onset. Subsequently, outliers in the remaining data (time * epochs) of each participant were identified and replaced by NaNs if their voltage value surpassed 5 standard deviations of all epochs at any time point. After baseline correction (200ms pre-stimulus baseline), the epoch data were submitted to statistical analyses. Note that these processes were performed upon non-NaN elements, while treating NaNs as missing values.

iEEG: time-frequency decomposition

For time-frequency analysis (TFA), we first bandpass-filtered the preprocessed traces between 0.5 and 200 Hz before segmenting epochs. Prior to epoch segmentation, outliers within each trace were identified and replaced with NaNs, following the same procedure as the event-related potential (ERP) analysis. After that, NaN values within traces were interpolated using the inpaint_nans.m function (https://www.mathworks.com/matlabcentral/fileexchange/4551-inpaint_nans), which uses a simple plate metaphor, before time-frequency decomposition.

The TFA decomposition was conducted using Morlet wavelets via the newtimef.m function of the EEGLAB toolbox. The length of the wavelet increased linearly from 3 cycles at 2 Hz to 54 cycles at 180 Hz, corresponding to a sliding window length of 1670 ms. This modified wavelet length was chosen to optimize the tradeoff between temporal resolution at lower frequencies and stability at higher frequencies. The TFA outputted complex values combining both amplitude and phase values for each time-frequency point, resulting in a 2-D plane with a log-spaced frequency dimension (60 bins from 2 to 180 Hz) and a linearly spaced time dimension sampled at 250 Hz (4ms resolution). In the dimension of time, this 2-D plane was segmented into epochs ranging from -600ms to 1000ms around image onset.

iEEG: neural oscillation power

For each complex value at every time-frequency point, we extracted the amplitude and calculated the power as the squared amplitude. The power values of each epoch were then z-normalized across time to reduce sensitivity to noisy trials and allow for comparison of power values across different

frequency bins. Subsequently, every normalized power epoch was baseline corrected using a 200-ms pre-stimulus baseline. Finally, the power values were averaged across frequencies to assess the change in mean band power following image onset for any frequency bands of interest. It is important to note that mask-evoked power change was specifically measured by blank control trials, which could have been removed via the contrast between image (masks plus image) versus blank control (masks only) trials, resulting in a clear measure tied to visible or invisible processing in either the attended or unattended condition.

To test whether inhibitory alpha band power during the pre-stimulus period was selectively allocated to the hemisphere ipsilateral to the peripheral visual stream, we contrasted contralateral versus ipsilateral trials on its oscillation power for each contact located in either the left or right hemisphere. Baseline removal and normalization across time were not conducted anymore. Instead, power values were normalized across epochs for each time point to scale the data while preserving the variance between trials. Since visual masks and the target image were arranged in different timing sequences between visible versus invisible trials (but in the same sequence within each), which might differently alter the temporal profile of alpha power activity, we performed this analysis in parallel for visible trials and invisible trials, respectively.

iEEG: responsive contacts

In the current era, a hotly debated topic regarding the mechanisms of consciousness (Koch, Massimini et al. 2016, Consortium, Ferrante et al. 2023) revolves around the functional differences between the frontal brain, particularly the frontal lobe, and the posterior brain, encompassing the occipital, temporal, and parietal lobes. Until this issue is resolved, elucidating the roles of more specific brain regions remains challenging. Hence, in this study, responsive contacts were selected from the gray matter of the four neocortical lobes (Occipital, Temporal, Parietal and Frontal lobes), while excluding those from white matter.

By definition, responsive contacts were defined as contacts significantly engaged in visual saliency processing. We thus used the visual saliency contrast (visible minus invisible) to screen for responsive contacts under either attended or unattended conditions. In terms of neural activity, responsive contacts were identified based on either event-related potential (ERP) responses contributed mainly by slow neural oscillations (here filtered between 0.5-30 Hz) or fast gamma oscillation (70-150 Hz) power responses whose activity correlates with local neuronal spiking (Nir, Fisch et al. 2007, Ray, Crone et al. 2008).

Taking the ERP activity as an example first. For each attention condition and timepoint, a saliency index was calculated using the algorithm introduced above. Subsequently, the visibility labels of epochs were randomly shuffled while keeping block membership and attention label unchanged, and saliency indices were recomputed using the same algorithm. This process was repeated 10,000 times to create a null distribution for each timepoint. The true saliency index was then ranked within the 10,000 surrogate distribution, with ranks of >=9995 or <=5 considered significant (corresponding to a two-tailed P <= 0.001). Timepoints showing significant activity were clustered across time, with clusters lasting >33ms considered responsive. Timepoints inside the identified clusters were coded as 1 while other timepoints outside as 0. The same procedure was conducted

for high gamma power in parallel with ERP analysis, resulting in another timeline of binary indices. For tach timepoint, above-chance contacts were defined as the union of contacts that turned out above-chance for either ERP or high gamma power analysis.

After that, for each timepoint, we summed the number of above-chance contacts from the four neocortex lobes of interest, resulting in a new timeline of summed N. To control for false alarms, we calculated the mean value (*n*) and standard deviation (*std*) across timepoints during the 500ms pre-stimulus baseline period. We then calculated a Z value for each timepoint using the formula:

$$Z_t = \frac{(N_t - n)}{std}$$

where N_t denotes the number of above-chance contacts for each timepoint. Responsive window included timepoints of a Z value >3 and falling within the range of [0 600]ms post-stimulus onset. Responsive window for the attended condition turned out much exceeding that for the unattended condition. For each attended and unattended condition, respectively, responsive contacts were identified as the union of above-chance contacts derived from all timepoints within the responsive window.

Reducing data homogeneity: electrode-level measures beyond contact-level measures

For each lobe, patients may have multiple electrodes implanted, with each electrode potentially containing multiple responsive contacts. It is well known that data of adjacent contacts coming from the same electrode are highly correlated. On the contrary, data of contacts from the same electrode but different lobes, as well as those from different electrodes but the same lobe, are much more heterogeneous. To control for data homogeneity, data from multiple responsive contacts coming from the same lobe and same electrode were averaged to calculate electrode-level neural activity. To further mitigate contamination from false alarm random noise, unless specified otherwise, we only included lobe-electrode units that contained n>=2 responsive contacts into further analyses. Similarly, imaginary coherence values were also computed between electrode-level pairs, with each electrode pair calculated as the mean of multiple included contact-level pairs. To control for false alarm, unless specified otherwise, we only included electrode pairs that contained n>=4 contact pairs into the formal coherence and coherence-based decoding analyses.

iEEG: functional coherence between responsive contacts

Between any two responsive contacts, functional coherence was calculated across time rather than across trials. This allowed us to assess the degree of phase clustering for each condition without necessarily requiring phase differences to cluster around the same angles across trials. On the other side, this also allowed us to better mitigate confounds introduced by uneven trial numbers across experimental conditions and participants, alongside artefacts stemming from inter-trial fluctuations in internal brain states and ongoing background neural activity. When combined with decoding analyses, notably, this trial-resolved coherence calculation further enabled us to independently assess the degree to which pair-wise coherence patterns encode saliency presence signals or saliency category signals.

More specifically, an approach based on imaginary coherence (Nolte, Bai et al. 2004), which is insensitive to volume conduction, was employed to mitigate the impact of a common input on

interregional neural synchronization (Karalis, Dejean et al. 2016, Chen, Tan et al. 2021). Using code from (Cohen 2014), imaginary coherence for each frequency was calculated as:

$$ImgC_{xy} = \frac{\left|Im\left(\sum_{n=1}^{n=N} S_{xy}\right)\right|}{\sqrt{\left(\sum_{n=1}^{n=N} S_{xx}\right) \cdot \left(\sum_{n=1}^{n=N} S_{yy}\right)}}$$

where S_{xy} denotes the cross-spectral density between activities at contacts x and y, S_{xx} and S_{yy} are the autospectral densities for contacts x and y, N denotes the number of time bins, and ImgC represents the absolute imaginary coherence. Cross- and autospectral densities were computed using time series of complex values obtained from Morlet wavelets introduced above (iEEG: time-frequency decomposition).

For each trial, ImgC was computed between any two contacts over 300 ms time segments in a sliding manner. The resulting values were then averaged across corresponding trials to obtain coherence measures for each combined condition across attention and visibility. In this study, six sliding time segments of a 300 ms window size were used: 0-300 ms, 100-400 ms, 200-500 ms, 300-600 ms, 400-700 ms, and 500-800 ms, to illustrate how coherence measures evolved over time.

The selection of time segment length involves a trade-off between signal-to-noise ratio and temporal precision. Longer time segments, encompassing more oscillation cycles, yield more robust and higher signal-to-noise estimates of phase synchronization. However, this comes at the expense of decreased temporal precision for time-varying and task-related modulations of phase synchronization, which are the main focus of this study. To reduce susceptibility to noise or nonrepresentative data, the resulting ImgC value for each condition was transformed to adjusted ImgC (Rayleigh's Z, using code from (Cohen 2014)) using the formula:

$$adj.ImgC = N * ImgC^2$$

where N is the number of timepoints. This calculation allows the resulting coherence values to exceed 1. A p-value can be computed from adj.ImgC to determine statistical significance (Cohen 2014).

iEEG: SVM-based decoding for image presence and image category

The decoding algorithm applied in this study consists of three elements: feature data, label data, and classifier models, which serve to categorize feature data into corresponding label groups. Specifically, Support Vector Machine (SVM) classifiers with a linear kernel were adopted for all decoding procedures in the present experiment. Classifiers were typically trained in a sliding bin manner (bin size = 25ms, step size = 15ms), with 10ms overlap between two neighboring bins. In this way, models were trained independently for each contact and each bin.

Without otherwise delineated, the feature data typically used for decoding were multi-variate, consisting of mean ERP response and the mean normalized power of six contiguous frequency bands (2-4, 4-8, 8-13, 13-30, 30-60, and 60-150 Hz), with all averaged within the bin. In other scenarios, feature data could also consist of some univariate measures, including phase coherence measures calculated for each trial, to better evaluate contribution of specific features. The configuration of label data was designed according to the research objectives, covering two decoding procedures:

binary decoding for image presence and trichotomous decoding for image category.

For image presence decoding, all experimental trials were enrolled and divided into two labels: image-present trials and image-absent blank control trials. Models were trained to judge the presence or absence of visual images under each combined condition of attention and visibility, with a theoretical chance level of 1/2. Considering that the number of image-present trials was twice that of image-absent blank control trials, a two-run training strategy was implemented for sample balance. In each run, non-overlapping half of the image-present trials were matched with control trials for model training, and the final decoding performance was averaged across the two runs. An 8-fold cross-validation scheme was adopted in each training run, where the total feature dataset was partitioned into eight equal subsets. In each validation fold, seven subsets were used for classifier training, and the remaining subset was used for model testing. This iterative process guaranteed that all samples were tested exactly once. Classifier performance was evaluated via decoding accuracy, calculated as the proportion of correctly classified samples to the total number of tested samples.

In comparison, image category decoding only adopted image-present trials for analysis (control trials were excluded due to the lack of visual stimuli), aiming to distinguish neural pattern differences among three predefined image categories, with a theoretical chance level of 1/3. Given the equal trial quantity across all category labels, model training was completed in a single run with the same 8-fold cross-validation method. Ultimately, the image category decoding accuracy under each of the four combined attention and visibility conditions was quantified using the same accuracy calculation criterion as the image presence decoding.

Visual saliency contrast

For both visible and invisible images, image-evoked ERP and neural oscillation power and phase-coherence measures were calculated by subtracting blank control trials consisting of pre- and post-masks only (blank trials) from trials consisting of both masks and image (image trials), obtaining a mask-free measure of image-evoked response linked to each condition. Using these mask-free measures (i.e., image minus blank), a visual saliency index was further quantified using the following algorithm (visible minus invisible).

$$Saliency = (Vis_{image} - Vis_{blank}) - (Inv_{image} - Inv_{blank})$$

Here, “Vis” and “Inv” denote visible and invisible trials, respectively. Under each attended or unattended conditions, this visual saliency contrast obtains a visual saliency index quantifying saliency-evoked response based on ERP and neural oscillation power and phase-coherence measures.

Saliency presence signal and Saliency category signal

This visual saliency contrast logic was also applied to image presence decoding measures (separating image vs. blank trials) and image category decoding measures (separating animal vs. object vs. face images). These decoding measures were first obtained for visible trials (Visible_Decod) and invisible trials (Invisible_Decod), and then made a contrast between them to quantify saliency presence signals (Saliency Presence) and saliency category signals (Saliency

Category), respectively, using following algorithms.

$$Salieny\ Presence = Visible_Decod_{(image|blank)} - Invisible_Decod_{(image|blank)}$$

$$Salieny\ Category = Visible_Decod_{(animal|object|face)} - Invisible_Decod_{(animal|object|face)}$$

Covering saliency presence and saliency category signals, as well as saliency-evoked ERP and neural oscillation measures, all these visual saliency contrast measures were calculated for each attended and unattended conditions, separately.

Attentional gain contrast

Though similar first-level saliency index measures had ever been used to evaluate neural correlates of consciousness (NCC) (Dehaene, Naccache et al. 2001, Cohen, Ortego et al. 2020), we were aware that this index cannot be directly interpreted as a measure of NCC due to its confounding with factors like stimulus intensity confounds (Lau 2022). To isolate NCC, instead, our main interest was on the second level 'attentional gain' contrast. This attentional gain contrast was performed between two attention conditions (attended minus unattended), so as to evaluate how top-down attention alters visual saliency processing and promotes visual consciousness as a result.

$$Attentional\ Gain = Saliency_{att} - Saliency_{unatt}$$

Here, "att" and "unatt" denote the attended and unattended conditions, respectively, and "Saliency" includes all visual saliency contrast measures introduced above. It is notable that, in behavior, attentional gain consists of not only explicit experience of visual consciousness but also post-perceptual response. One of the major strengths of the present study is that we have isolated consciousness-related attentional capture process while excluding confounding from preconscious preparation before attentional capture and post-perceptual response after attentional capture (see the main text).

Statistics

As introduced above, all statistics were performed on electrode or electrode-pair level (beyond contact level) to reduce homogeneity. Considering each lobe-electrode or lobe-electrode pair as an independent sample, parametric tests used included one-way and two-way repeated measures analysis of variance (ANOVA), paired-sample t-test, one-sample t-test, as well as Pearson and Spearman correlation analysis. Without otherwise denoted, all statistical tests were conducted in a two-tailed manner with a threshold of $p = 0.05$. The FDR correction or cluster-based permutation test was used to correct for multiple comparisons with a threshold of corrected $p = 0.05$.

To replicate findings, we also conducted linear mixed effects (LME) models with conditions of interest (e.g., visibility and/or attention) as fixed effects, and with patient and electrode membership (not individual contacts) as random effects. Using the restricted maximum likelihood method to estimate LME parameters, and using Bonferroni correction to correct for multiple comparisons (corrected P=0.05), the LME-based approach, which requires significantly more calculations, resulted in similar findings (not shown here for simplicity) as those reported here.

Additionally, as shown in Fig.**5e** of the main text, we investigated a U-shape relationship between theta coherence (i.e., the predictor, referred to as x) and coherence-based saliency presence decoding performance (i.e., the dependent variable, referred to as y), where x was a vector of electrode pairs measuring saliency-evoked change of mean theta coherence values (visible-invisible) and y was a vector of the same length measuring to what extent theta coherence values could discriminate between visible versus invisible trials (using univariate SVM models). Both x and y were calculated using data within the early window (0-300ms) at the posterior brain. Methodologically, this U-shape line was drawn based on a simulation fitting a quadratic polynomial curve to the data which was completed using the fit.m function in MATLAB with a fittype of 'poly2'. This function takes the form f(x) = p1*x^2 + p2*x + p3, where p1, p2, and p3 are the coefficients of the polynomial. The fit.m function finds the best-fitting polynomial curve to the data points, minimizing the sum of the squares of the differences between the data points and the curve. Though this approach testing U-shaped functions via quadratic regressions is widely used, it imposes an arbitrary functional-form assumption that in some scenarios can lead to a 100% rate of false positives (e.g., the incorrect conclusion that y = log(x) is U shaped). As a more rigorous means to test for this U-shape relationship without a functional-form assumption, the two-lines test (Simonsohn 2018) was used to further test this U-shaped relationship (see Fig.**S13** for more methodological details and interpretations).

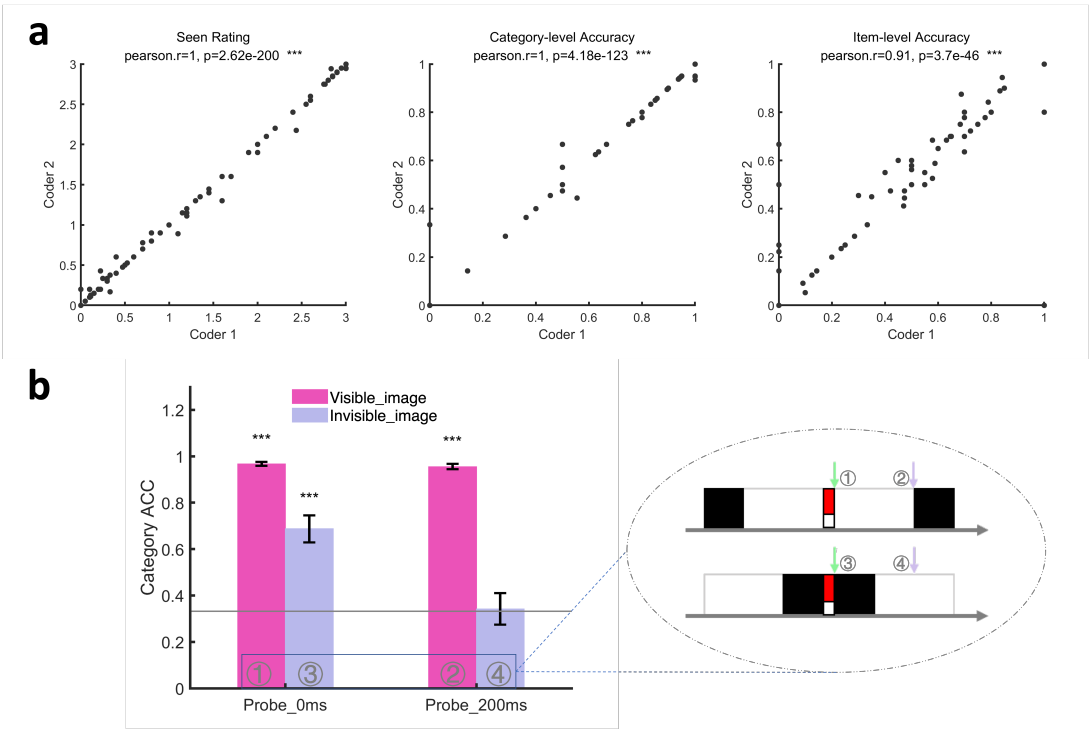


Fig.S1. Coding and validation for participants' oral report of Exp.1. a, For each audio record of participants' oral report in probe trials, two independent coders (Coder 1 and Coder 2) coded visibility rating (left panel, from 0 = "definitely unseen" to 3 = "definitely seen"), category-level accuracy (i.e., category ACC, middle panel) and item-level accuracy (right panel) with high reliability. Each dot represents a mean coding for a given image type from a single participant. Pearson correlation analysis revealed near to perfect reliability between two coders. **b**, Mean category ACC varied with four combined conditions (i.e., condition 1~4) of visual mask and probe timing (as shown in the amplified inset). In condition 1 and 2 where images (red rectangles) were weakly masked, neighbored with blank period interval (white rectangles), optimal accuracy evidenced they were truly visible. By contrast, in condition 4 when images were closely masked by both the forward and the backward masks (black rectangles), the chance-level accuracy suggests that they were completely invisible. In condition 3 when images were masked by forward mask only (the backward mask had not yet been presented, see the inset for the timing structure), the above-chance moderate accuracy suggests there preserved some residual awareness for the presented image due to absence of backward masking. *, $p<0.05$; **, $p<0.01$; ***, $p<0.001$.

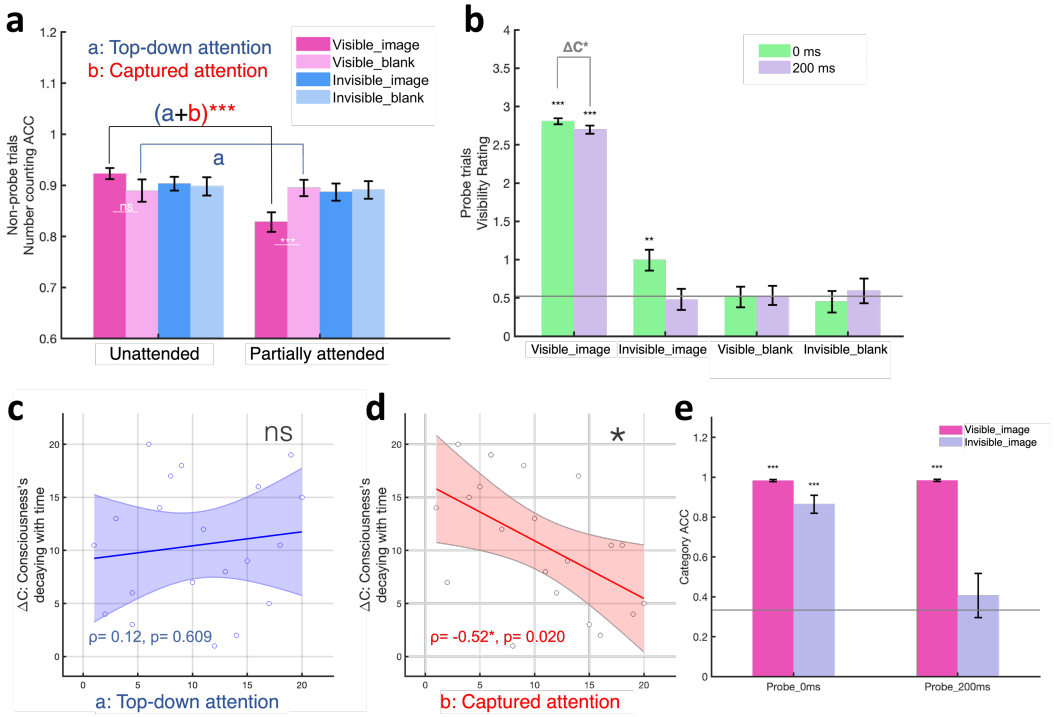


Fig.S2. Independent replication for Exp.1's main finding reported in the main text. To further test for the link between captured attention and conscious experience, a follow-up experiment was designed and performed using roughly the same paradigm and comparable sample size (20 healthy colleague students, 16 females, age=23.1 ± 1.88 years) but recruiting a different experimenter and two new audio encoders. The major difference lied in the instruction that we provided for participants. That is, we required them to more strictly set priority the counting task and strictly avoid being distracted by peripheral images as best as they can. In extreme cases, it was even acceptable for one to perceptually miss all the images nested in probe trials only if they best directed their attention to counting. Otherwise, if attentional distraction occurred a decrease of counting performance would lead to a decrease of their monetary reward they received at last (note that this 'punishment' rule served only as a cover story which did not work in reality). In this way, we aimed to further test the relationship between captured attention and conscious experience in the scenario when the amount of top-down attention is largely diminished.

a, In the unattended condition (i.e., without probe), counting performance did not vary with visibility ($F_{(3, 57)}$= 1.32, p=0.277, η_p^2=0.065), confirming that in the unattended condition peripheral salient images failed to capture attention. In the partially attended condition (i.e., with probe), though there was a general decrease ($t_{(18)}$=-2.22, p=0.038) on counting performance relative to the unattended baseline, this general decrease was mainly contributed by visible_image trials, whereas performance for visible_blank, invisible_image or invisible_blank trials exhibited no significant decrease relative to the unattended baseline (uncorrected p>0.1) after we strictly required participants to avoid being distracted. This finding indicates that, expectedly, the amount of top-down attention had largely diminished to a minor level (non-detectable). If visible image was shown, however, we replicated the effect of attentional capture even in the near absence of top-down attention (also see (Li, VanRullen et al. 2002)). That is, visible_image trials relative to invisible_image trials drastically encountered an additional decrease of task performance

(interaction: $F_{(1, 19)}$=14.89, p=0.001, η_p^2=0.439) which was irrespective of categorical contents ($F_{(2,38)}$=0.44, p=0.650, η_p^2=0.023), confirming that when the image became task-relevant and thus attention became available, visibility-related (visible versus invisible) signal automatically and additionally captured attention. Together with Exp.1 reported in the main text, findings here further lead to the conclusion that top-down attention and bottom-up attentional capture are two distinct processes. Following prior procedure, we subtracted the amount of attention generally divided to visible_blank trials (component a: top-down attention, $t_{(19)}$=-0.28, p=0.786, Cohen's d=0.06) from that of visible_image trials (component a+b: top-down plus captured attention, $t_{(18)}$=5.13, p<0.001, Cohen's d=1.15) to avoid any confounding from masks, thus obtaining a clean measure of the amount of captured attention (component b). Following results confirm that it is the captured attention that contributes to conscious experience.

b, For 16% probe trials, the decrease of visibility rating ($t_{(19)}$=-2.82, p=0.011, Cohen's d=0.63) for 200ms versus 0ms probes was observed again, indicating that the consciousness trace was decaying over a 200ms temporal gap. When images were masked by forward mask only (i.e., 0ms probe tests from the invisible_image trials, where the backward mask had not yet been presented), the above-chance moderate accuracy suggests there preserved some residual awareness for the presented image due to absence of backward masking.

c and **d**, Most importantly, we replicated the main finding that the magnitude of consciousness's decaying over time was negatively correlated with the amount of captured attention (spearman ρ= -0.52, p=0.020) but nonsignificant for top-down attention (spearman ρ= 0.12, p=0.609).

e, Validation for participants' oral report from this replication experiment. In line with Fig.**S1b**, optimal category ACC proved visible images were consciously perceived in both 0ms and 200ms probe tests (two red-pink bars). Chance-level ACC (i.e., 0.33, light blue bar at Probe_200ms condition) proved the masking by the forward and the backward masks had successfully rendered the target image invisible. When images were masked by forward mask only (i.e., the light blue bar at Probe_0ms condition, where the backward mask had not yet been presented), the above-chance moderate accuracy suggests there preserved some residual awareness for the image due to absence of backward masking. ns, p>0.05; *, p<0.05; **, p<0.01; ***, p<0.001.

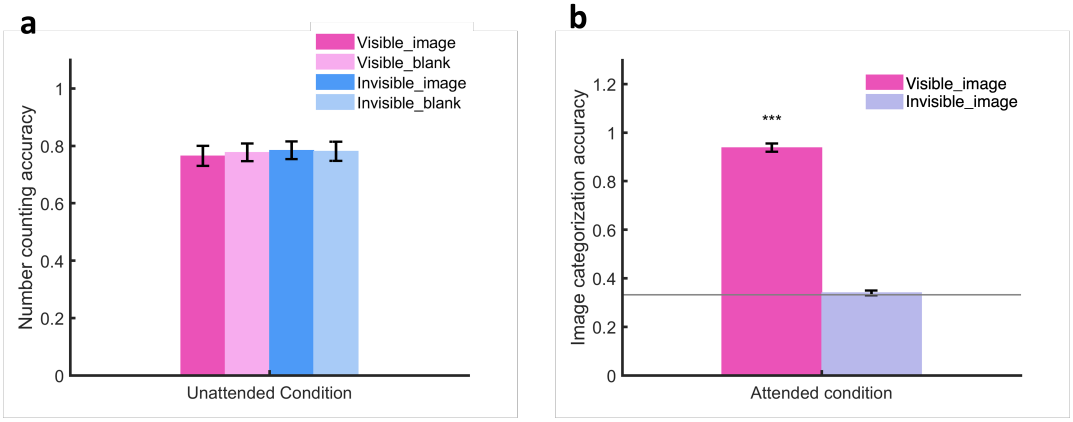


Fig.S3. Performance of the number-counting task and image categorization task by epilepsy patients of Exp.2. a, In the unattended condition, number-counting performance did not vary between four legend conditions ($F_{(3,\ 54)}$= 0.95, p=0.424, η_p^2=0.050), and performance for visible_image trials did not differ with that for its matched control (visible_blank, $t_{(18)}$=-1.00, p=0.328). These results collectively suggest that salient signal failed to capture attention in the unattended condition of Exp.2, agreeing well with the unattended condition results of Exp.1. **b**, In the attended condition, patients performed an image categorization task instead. Categorization accuracy was tested against the chance level (1/3) using one-sample t-test, revealing optimal accuracy for visible images ($t_{(18)}$=35.41, p=4.25e-18, Cohen's d=8.12) and chance-level accuracy for invisible images ($t_{(18)}$=0.99, p=0.335, Cohen's d=0.23). These results convinced us that visual masking was successful and in the attended condition patients did pay sufficient attention to peripheral image as expected. ***, p<0.001. Error bar represents SEM across patients.

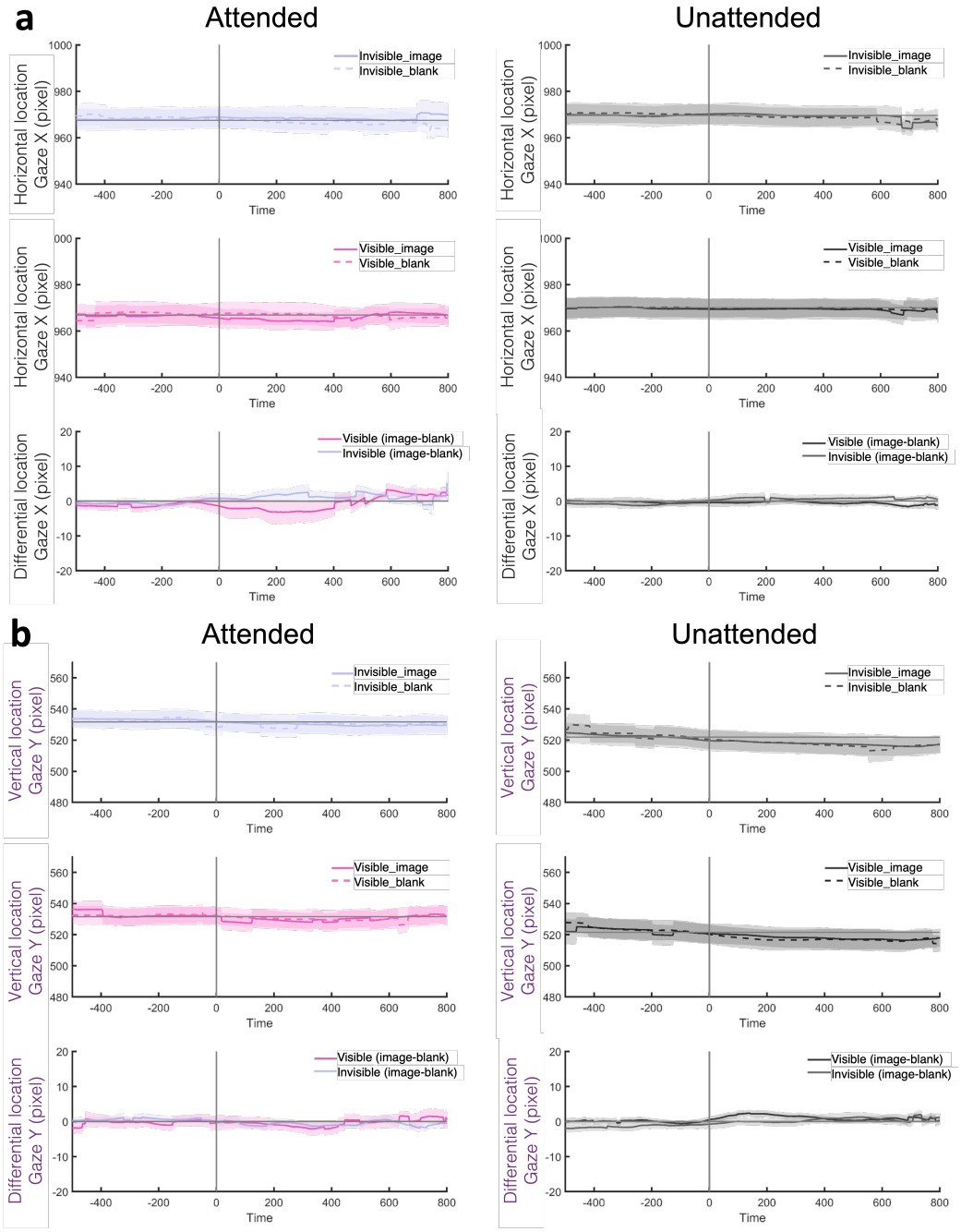


Fig.S4. Equivalent eye gaze location between image trials and blank control trials. For each horizontal gaze location (GazeX, **a**) and vertical gaze location (GazeY, **b**), and for each attended (left) and unattended condition (right), mean gaze location was illustrated and contrasted between image trials and blank control trials to quantify any image-induced change on gaze location. This procedure was performed for invisible images (row 1), visible images (row 2) and their contrast (row 3). Zero point in the X-axis denotes the onset of target image. To detect any difference during the pre-stimulus period, baseline correction was not conducted for this analysis on raw gaze location. As a result, no timepoint passed a liberal threshold of uncorrected $p<0.05$. As shown in the third row ('Contrast'), there was no significant difference between the visible and invisible images (uncorrected $p>0.05$), indicating their differential neural activity (i.e., the visual saliency contrast) reported in the main text was not contaminated by eye gaze distribution.

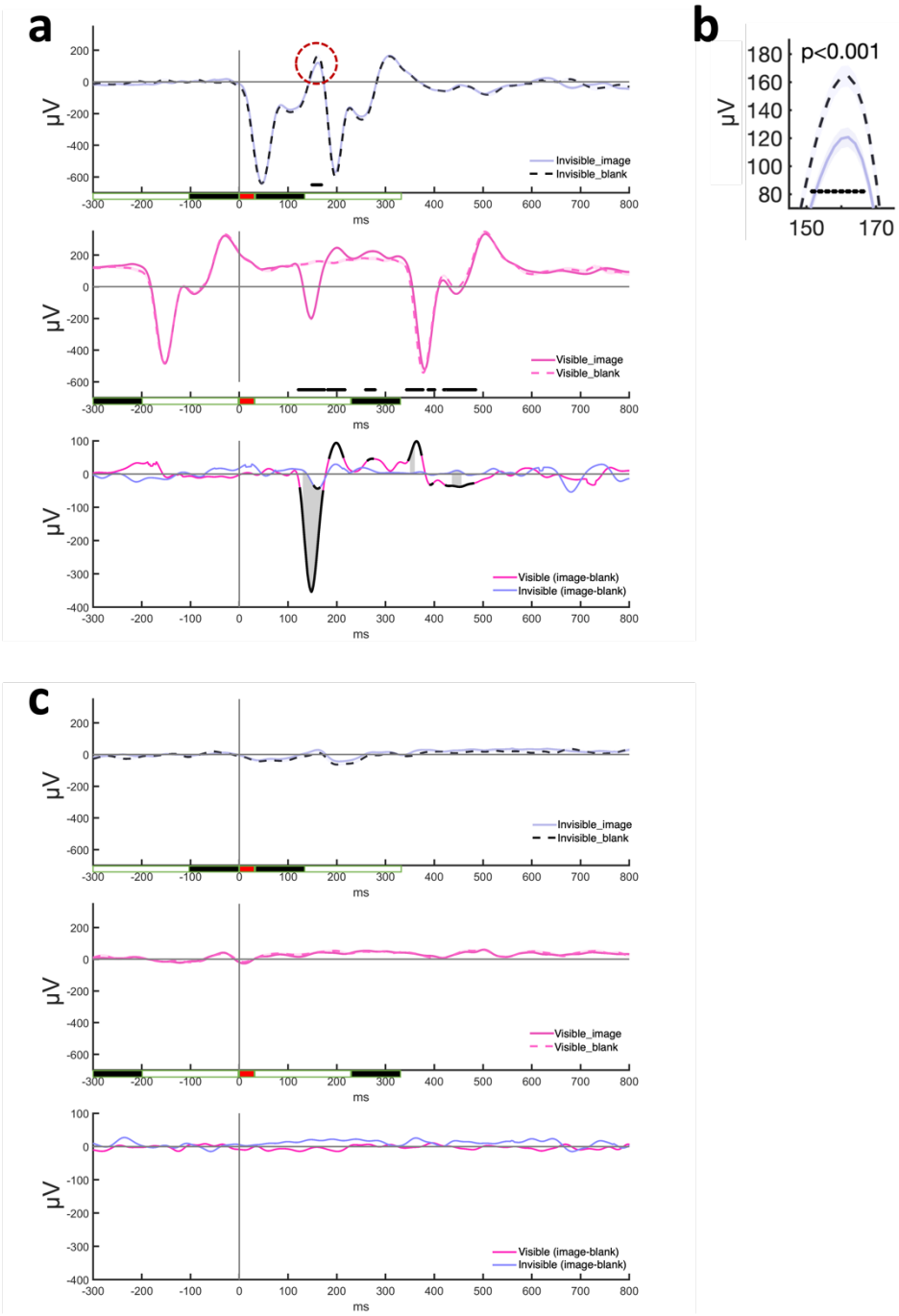
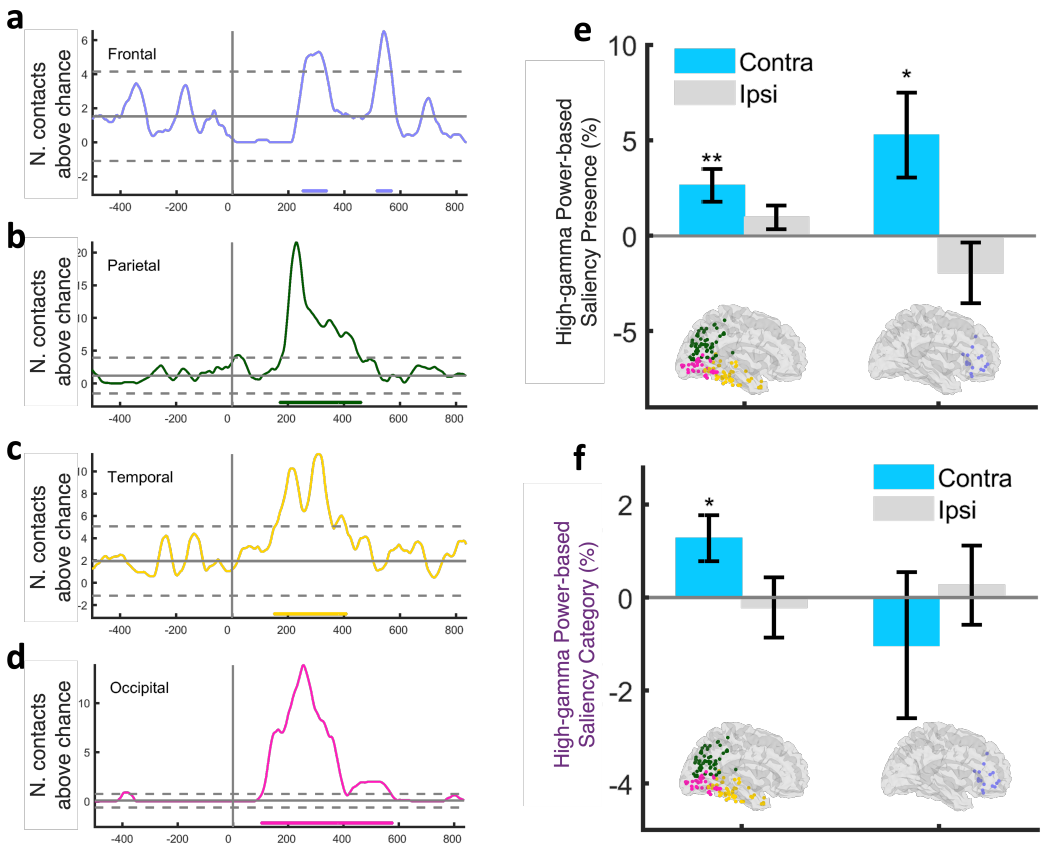


Fig.S5. iERP response of a representative V1 contact in the unattended condition. The upper and middle rows show V1 response to invisible and visible images, respectively, by evaluating the difference between solid and dotted lines. Tied to the x-axis, rectangles face-colored in white, black and red indicate the presentation of a blank screen, a visual mask and a target image (or its blank control), respectively. Note that the dotted lines indicate background iERP activity evoked by masks only. The bottom row compared V1 response to visible versus invisible images with each subtracting the background iERP. Cluster-based permutation test revealed no clusters showing significant difference between two lines for each panel (corrected $p > 0.05$). This result suggests that, without attention, V1 could be largely non-responsive to the peripheral visual stream displayed in the ipsilateral visual field.



644

645 **Fig.S6. Cortical distribution and local signal encoding of responsive contacts under**
646 **unattended conditions. a-d**, Time course of number of contacts (N. contacts) exceeding the
647 baseline chance level for frontal (F), parietal (P), temporal (T) and occipital (O) lobes under
648 unattended conditions. Gray dotted lines indicate 95% confidence interval of baseline (from -500ms
649 to 0ms) variation. Colored lines onto X-axis indicate time points showing significant more contacts
650 exceeding the chance level ($p<0.05$). **e-f**, High-gamma power-based decoding for saliency presence
651 signal (**e**) and saliency category signal (**f**). This decoding was performed separately for contralateral
652 (Contra) and ipsilateral (Ipsi) hemisphere response using responsive contacts under unattended
653 condition. Colored dots projected onto the brain illustrate location of responsive contacts from the
654 posterior brain (left) and the frontal brain (right) . *, $p<0.05$; **, $p<0.01$.

655

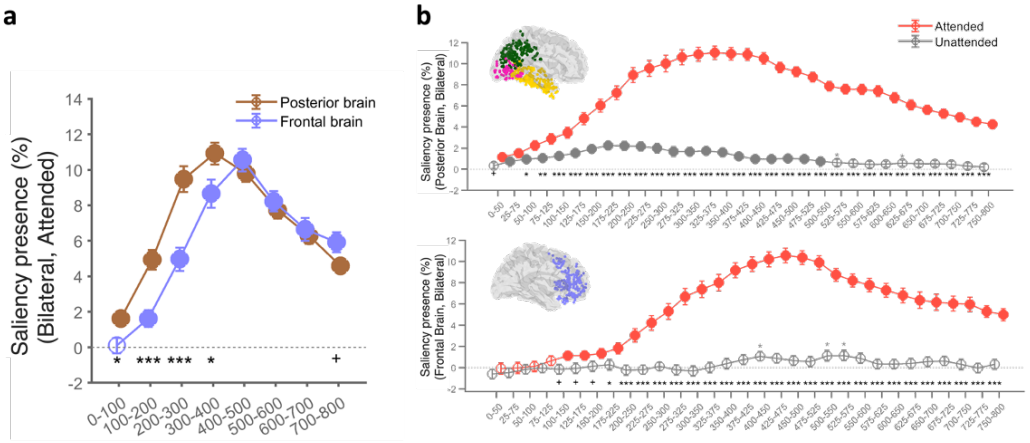


Fig.S7. Time course of saliency presence signals of the posterior brain and the frontal brain. **a**, Saliency presence signals represented by the posterior brain and the frontal brain under attended conditions. **b**, More fine-grained time course (50ms bin size, 25ms overlap between neighbor bins) under both attended and unattended conditions using responsive contacts identified at the attended condition. In each plot, the filled circles represent significant difference versus 0 (FDR corrected $p<0.05$), asterisks above empty circles represent uncorrected $p<0.05$. Asterisks alongside the X-axis indicates significant difference between two legend conditions according to uncorrected p values. +, p<0.1; *, p<0.05; **, p<0.01; ***, p<0.001. Error bar represents SEM.

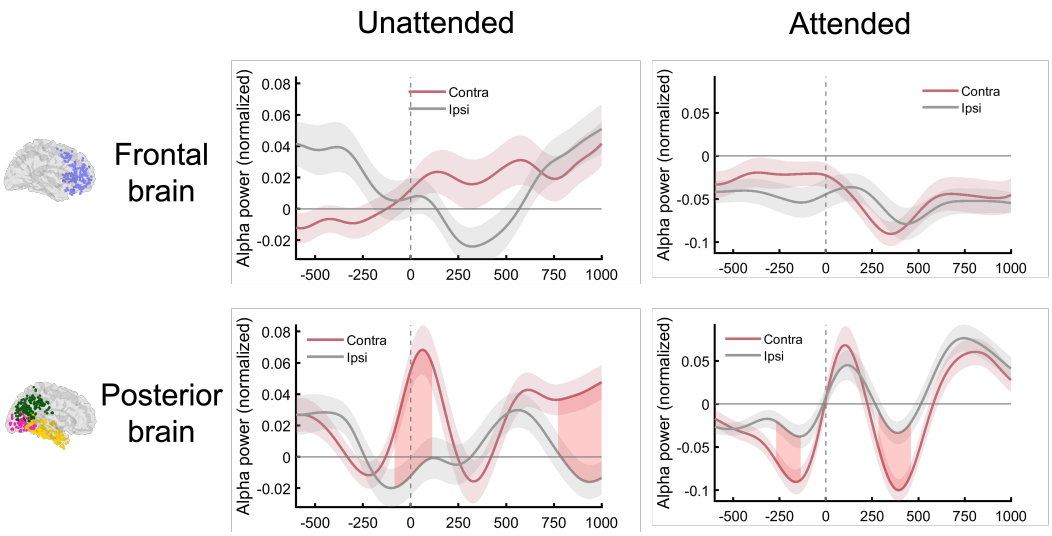


Fig.S8. Pre-stimulus alpha-band activity for invisible trials. Normalized alpha power (without baseline removal) was compared between contralateral vs. ipsilateral hemispheres for each combined conditions of posterior/frontal brain and attended/unattended conditions. Zero point in the x-axis indicates image onset. Shaded area around lines represents SEM. Shaded area between lines indicates significant difference (cluster-based permutation corrected $p<0.05$). See Fig.**3c** of the main text for pre-stimulus alpha-band activity for visible trials.

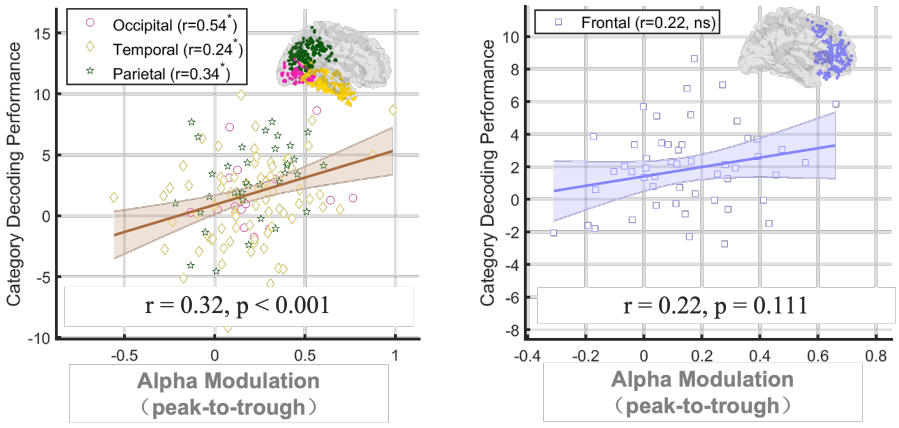
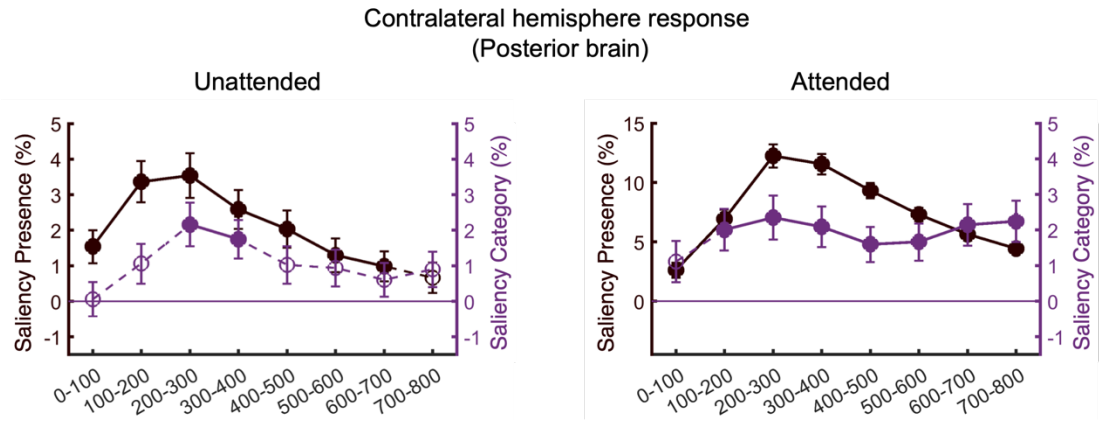


Fig.S9. Correlational relationship between saliency-evoked alpha-band modulation and saliency category signal under the attended condition. For the posterior brain (left), a peak-to-trough (bin 3 vs. bin 6) alpha modulation index was calculated and then imported into correlation analysis with mean category decoding accuracy. This correlational analysis was also performed for each individual lobe in the posterior brain (i.e., the occipital lobe, temporal lobe and the parietal lobe, as shown in the legend box). For the frontal brain (right, i.e., the frontal lobe), this analysis was performed with the alpha modulation index calculated between bins with peak (bin 4) vs. trough (bin 7) values. See Fig.**3d** of the main text for different timing profiles about peaks and troughs of the posterior brain vs. frontal brain. *r*, Pearson correlation coefficient; *ns*, non-significant. *, uncorrected p<0.05.



S10. Contralateral hemisphere response of the posterior brain on unattended and attended conditions. Under unattended (left) and attended (right) conditions, saliency presence and saliency category signals encoded by the contralateral hemisphere of the posterior brain were depicted into a pair of 2-Yaxes plot. Filled circles indicate significant difference versus 0 (FDR corrected $p<0.05$; corrected $p>0.05$ for empty symbols). X-axis tick labels represent time bins (100ms bin size) relative to image onset, in unit of ms. The error bars represent the SEM.

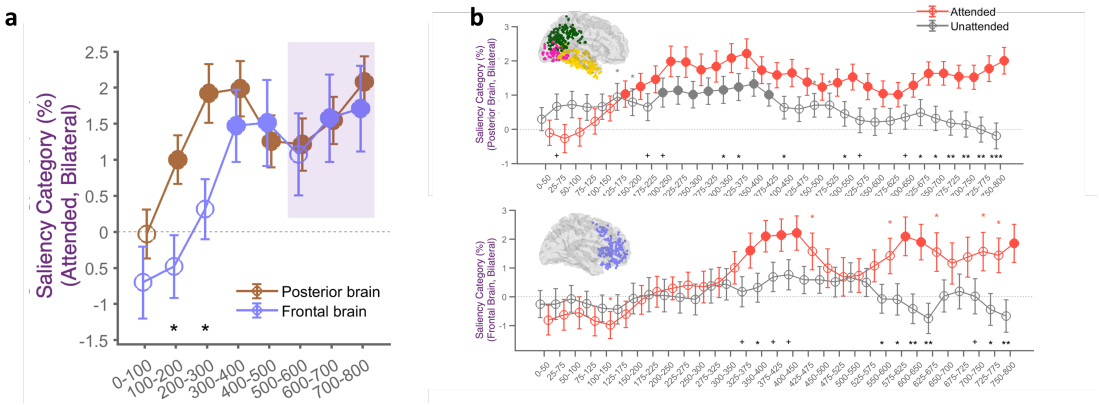


Fig.S11. Time course of saliency category signals of the posterior brain and the frontal brain. **a**, Saliency category signals represented by the posterior brain and the frontal brain under attended conditions. The purple-shaded area indicates concurrent late retrieval of saliency category signals in both these two modules. **b**, More fine-grained time course (50ms bin size, 25ms overlap between neighbor bins) under both attended and unattended conditions using responsive contacts identified at the attended condition. In each plot, the filled circles represent significant difference versus 0 (FDR corrected $p<0.05$), asterisks above empty circles represent uncorrected $p<0.05$. Asterisks alongside the X-axis indicates significant difference between two legend conditions according to uncorrected p values. +, p<0.1; *, p<0.05; **, p<0.01; ***, p<0.001. Error bar represents SEM.

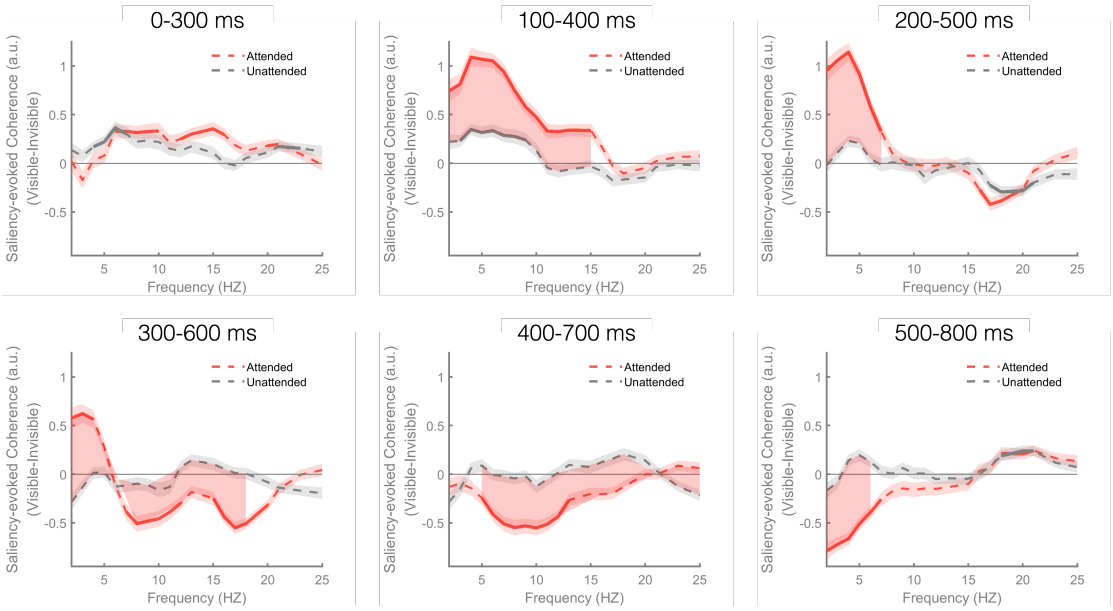


Fig.S12. Saliency-evoked coherence changes under attended and unattended conditions. Note that this coherence measure was calculated as adjusted imaginary coherence which may produce values exceeding 1 (See Method for more details). For each condition and each bin of 300ms window size, we averaged saliency-evoked coherence values across all electrode pairs (not contract pairs, see Fig.**5a** of the main text to control for data homogeneity). Solid lines indicate significant change (cluster-based permutation test, $p<0.05$). Dotted lines indicate non-significant results (cluster-based permutation test, $p>0.05$). Shaded area around each curve represents SEM. Shaded area between curves indicates significant difference between the attended and unattended conditions (cluster-based permutation test, $p<0.05$). Note that during the positive coupling bins under attended conditions (100-400ms, 200-500ms, and 300-600ms bins), the strongest coupling intensity peaked at around 4HZ.

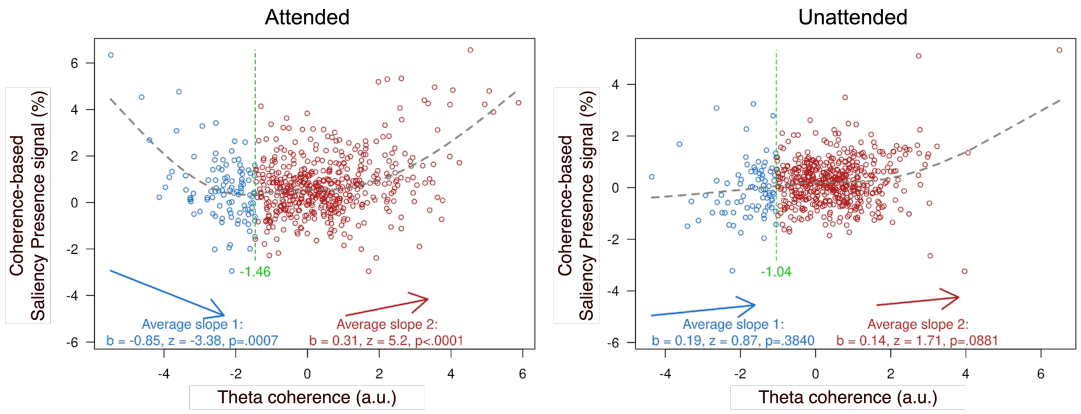


Fig.S13. Two-lines test for the U-shape relationship between theta coherence and coherence-based saliency presence signal. This test is supplemented to Fig.**5e** of the main text, where we investigated a U-shape relationship between theta coherence (i.e., the predictor, referred to as x) and coherence-based saliency presence decoding performance (i.e., the dependent variable, referred to as y). In the main text, this U-shape line was drawn based on a simulation fitting a quadratic polynomial curve to the data which was completed using the fit.m function in MATLAB with a fittype of 'poly2'. Though this approach testing U-shaped functions via quadratic regressions is widely used, it imposes an arbitrary functional-form assumption that in some scenarios can lead to a 100% rate of false positives (e.g., the incorrect conclusion that y = log(x) is U shaped).

As a more rigorous means to test for this U-shape relationship without a functional-form assumption, the two-lines test (Simonsohn 2018) was used to further test this U-shaped relationship. Basically, this approach estimates two regression lines, one for low and one for high values of x. A breakpoint xc was first set using a "Robin Hood" algorithm which seeks to obtain higher power to detect a u-shape if it is present. More details and an application procedure for running the two-lines test are available at http://webstimate.org/twolines. After setting a breakpoint, the two-lines test runs two interrupted regressions, one which includes the breakpoint in the first segment, then one which includes it in the second. Each regression results in a parameter slope b, as well as another two Z and p values evaluating its statistical significance. If the resulting two slopes have opposite sign, and are individually statistically significant, the test rejects the null hypothesis that there is no u-shaped (nor inverted u-shaped) effect.

As a result, in the attended condition (left panel), we found that the first line (blue arrow) had negative slope while the second line (red arrow) had positive slope, and both slopes were statistically significant ($p<0.001$). By contrast, in the unattended condition (right panel), the slope of the first and the second lines were both positive, and neither of them reached statistical significance ($p>0.05$). Collectively, the U-shape relationship indeed existed but only existed in the attended condition. This finding implies that attention initiates a functional reorganization process at the posterior brain, rendering functionally coupled (positive coherence) and decoupled pairs (negative coherence) simultaneously detecting the presence of conscious signals at the 0-300ms early bin.

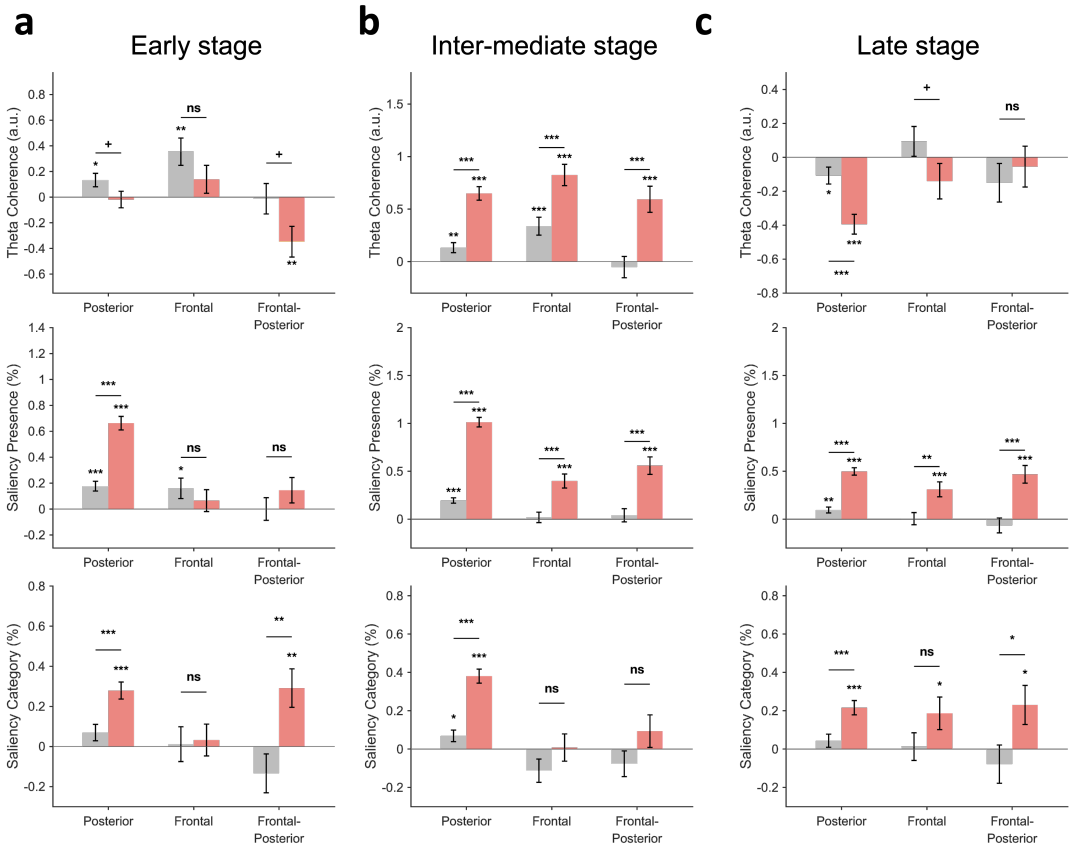


Fig.S14. Coherence and Coherence-based decoding for three groups of interest across (a) the early stage, (b) the intermediate stage, and (c) the late stage. For each of the three indices (upper row: theta coherence; middle row: coherence-based saliency presence signal; bottom row: coherence-based saliency category signal), and for each stage and each group, the unattended condition (gray bars) and the attended condition (red bars) were further compared with 0 each and mutually compared between each other. As reported in the main text, our most critical finding is that during the intermediate stage the Frontal group and the Frontal-Posterior group did not encode saliency category signal. To avoid missing potential signals (i.e., the Type II error), the correction for multiple comparisons, which is typically used to control for false alarms (i.e., the Type I error), were not performed. The statistical significance was thus marked according to uncorrected p values. +, $p<0.1$; *, $p<0.05$; **, $p<0.01$; ***, $p<0.001$. The error bars represent the SEM.

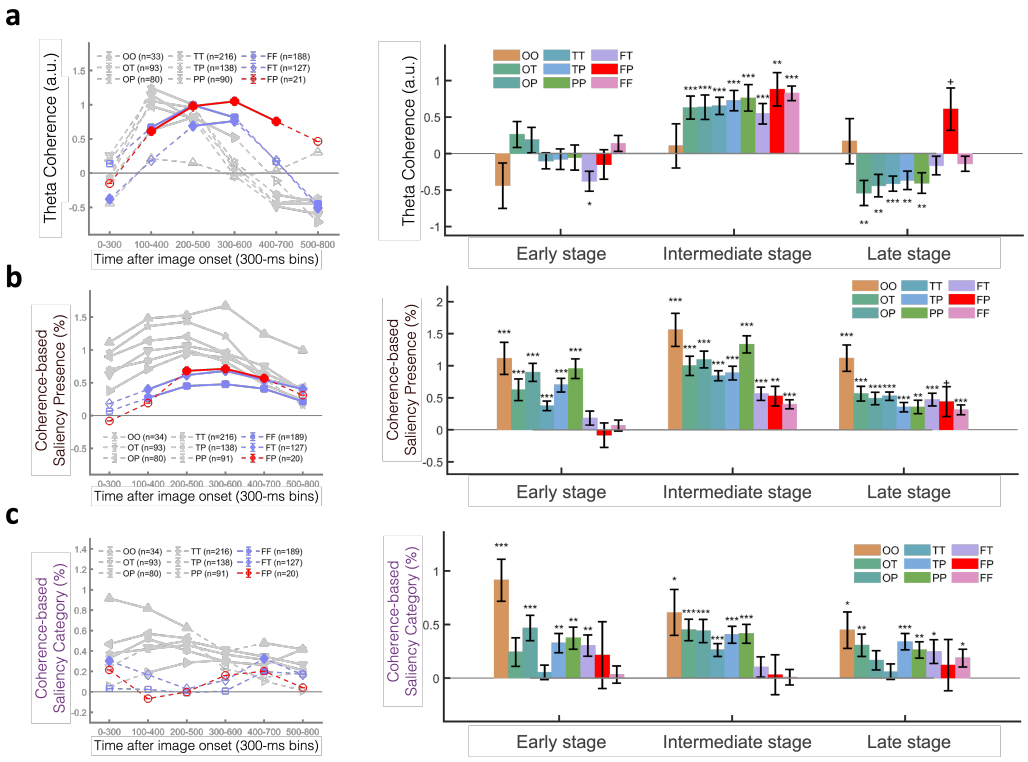


Fig.S15. Temporal dynamics of (a) theta coherence, (b) coherence-based saliency presence signals, and (c) coherence-based saliency category signals under the attended conditions. For each panel, the time course for each lobe pair spanning across 6 time-bins (left) and three identified stages (right) were shown in parallel. Filled symbols (left) and asterisks onto bars (right) indicate significant difference from 0 (FDR corrected $p<0.05$). +, corrected $p<0.1$; *, corrected $p<0.05$; **, corrected $p<0.01$; ***, corrected $p<0.001$. Without otherwise denoted, all X-axis tick labels represent time relative to image onset in unit of ms. The error bars represent the SEM.

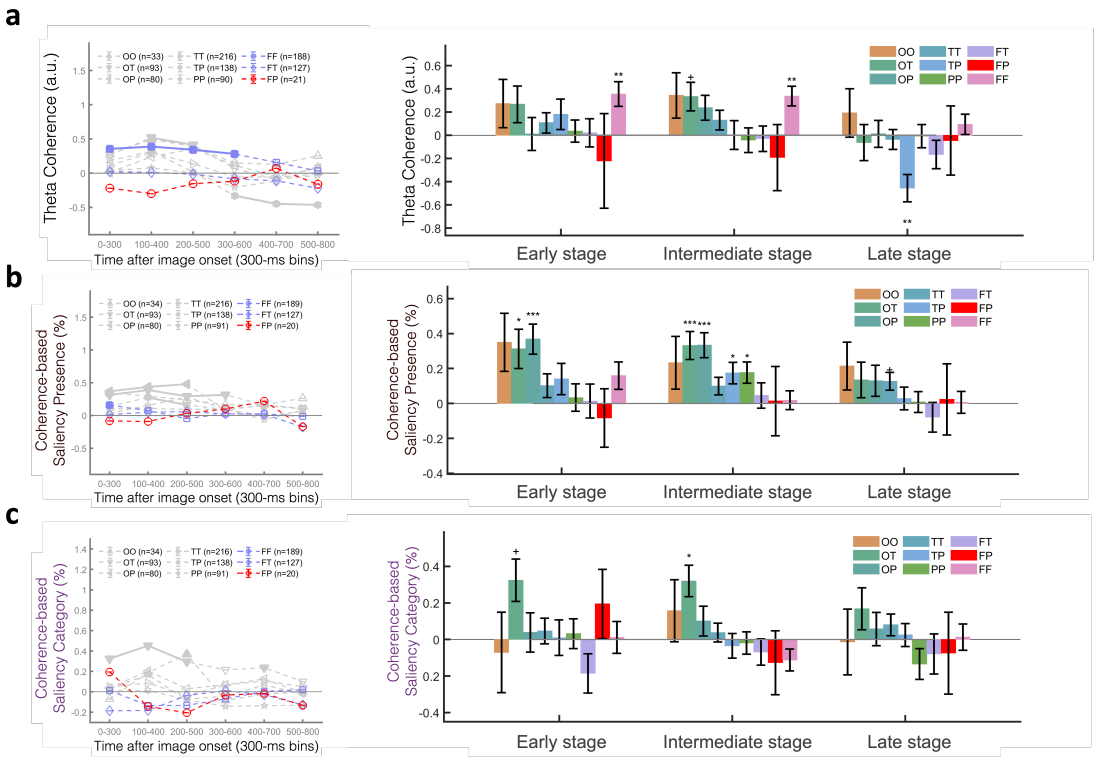


Fig.S16. Temporal dynamics under the unattended condition of (a) theta coherence, (b) coherence-based saliency presence signals, and (c) coherence-based saliency category signals. For each panel, the time course for each lobe pair spanning across 6 time-bins (left) and three identified stages (right) were shown in parallel. Filled symbols (left) and asterisks onto bars (right) indicate significant difference from 0 (FDR corrected $p<0.05$). +, corrected $p<0.1$; *, corrected $p<0.05$; **, corrected $p<0.01$; ***, corrected $p<0.001$. Without otherwise denoted, all X-axis tick labels represent time relative to image onset in unit of ms. The error bars represent the SEM.

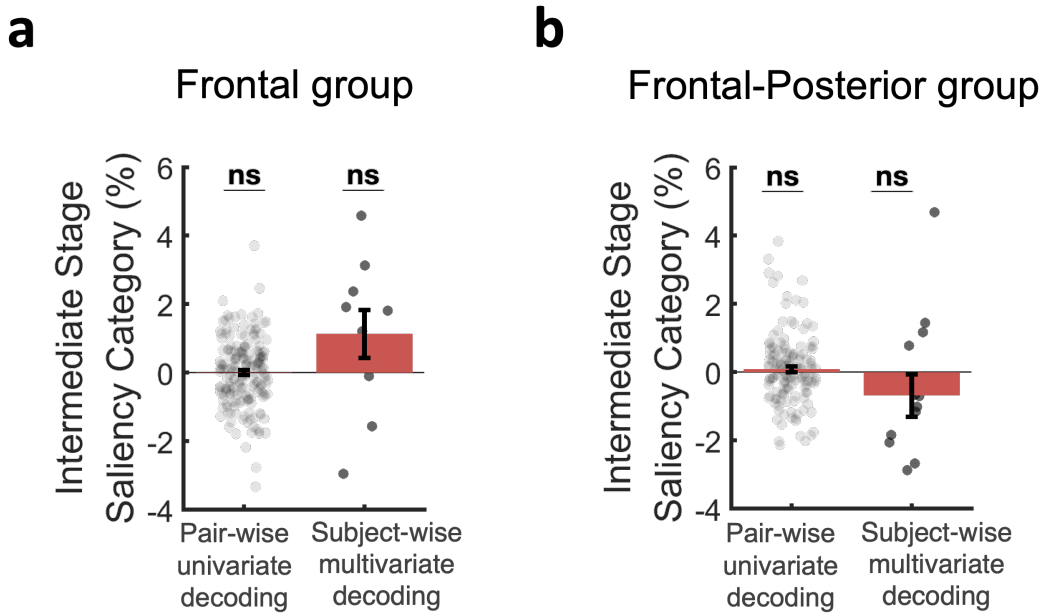


Fig.S17. Coherence-based decoding for saliency category signals of (a) the Frontal group and (b) the Frontal-Posterior group. To highlight non-significant decoding for saliency category signals reported in the main text, subject-wise multivariate decoding results (right) were concurrently displayed with the pair-wise univariate decoding (left). Each light-gray point on left bars represents an electrode pair (averaged across elementary contact pairs to control for data homogeneity, see Fig.**5a** of the main text), whereas each dark-gray point on right bars represents an individual patient.

Table S1. The information regarding the number of responsive contacts.

Patients	Occipital	Temporal	Parietal	Frontal	OTPF	ALL
SUB001	9/15	10/42	15/17	0/0	34/74	120
SUB002	0/0	12/56	9/23	0/0	21/79	128
SUB003	5/9	12/23	50/78	0/0	67/110	168
SUB004	0/0	12/78	7/13	1/12	20/103	160
SUB005	0/0	32/61	0/0	18/38	50/99	144
SUB006	0/0	14/38	0/0	19/53	33/91	136
SUB007	0/0	3/39	0/0	11/50	14/89	160
SUB008	0/0	1/18	8/41	9/15	18/74	160
SUB009	0/0	0/0	9/22	1/1	10/23	92
SUB010	0/0	3/12	9/17	27/49	39/78	132
SUB011	11/21	15/64	8/18	0/0	34/103	152
SUB012	5/5	57/68	14/16	0/0	76/89	144
SUB013	6/6	11/18	45/59	0/0	62/83	120
SUB014	0/0	16/61	0/0	27/33	43/94	140
SUB015	0/0	2/6	0/0	21/86	23/92	148
SUB016	0/0	47/104	0/0	24/32	71/136	192
SUB017	32/46	19/40	25/36	0/0	76/122	176
SUB018	0/0	0/0	0/0	37/123	37/123	156
SUB019	0/0	0/9	1/3	12/53	13/65	168
SUB020	17/28	20/27	19/41	0/0	56/96	128
SUB021	0/0	48/74	2/3	0/0	50/77	120

Movie S1.

Demo illustration of trials without any probes displayed in the unattended blocks (number-counting task) of Exp.1.

Movie S2.

Demo illustration of trials with randomly selected probes displayed in the partially attended blocks (number-counting task with occasional probes) of Exp.1.

Movie S3.

Demo illustration of trials displayed in the unattended blocks (number-counting task) of Exp.2.

Movie S4.

Demo illustration of trials displayed in the fully attended blocks (image-categorization task) of Exp.2.

Movie S5.

Spatial distribution of responsive contacts across four cortical lobes and across time.

Supplementary Reference

Brainard, D. H. (1997). "The Psychophysics Toolbox." Spat Vis **10**(4): 433-436.

Chen, S., Z. Tan, W. Xia, C. A. Gomes, X. Zhang, W. Zhou, S. Liang, N. Axmacher and L. Wang (2021). "Theta oscillations synchronize human medial prefrontal cortex and amygdala during fear learning." Science advances **7**(34): eabf4198.

Cohen, M. A., K. Ortego, A. Kyroudis and M. Pitts (2020). "Distinguishing the Neural Correlates of Perceptual Awareness and Postperceptual Processing." J Neurosci **40**(25): 4925-4935.

Cohen, M. X. (2014). Analyzing neural time series data: theory and practice, MIT press.

Consortium, C., O. Ferrante, U. Gorska-Klimowska, S. Henin, R. Hirschhorn, A. Khalaf, A. Lepauvre, L. Liu, D. Richter, Y. Vidal, N. Bonacchi, T. Brown, P. Sripad, M. Armendariz, K. Bendtz, T. Ghafari, D. Hetenyi, J. Jeschke, C. Kozma, D. R. Mazumder, S. Montenegro, A. Seedat, A. Sharafeldin, S. Yang, S. Baillet, D. J. Chalmers, R. M. Cichy, F. Fallon, T. I. Panagiotaropoulos, H. Blumenfeld, F. P. d. Lange, S. Devore, O. Jensen, G. Kreiman, H. Luo, M. Boly, S. Dehaene, C. Koch, G. Tononi, M. Pitts, L. Mudrik and L. Melloni (2023). "An adversarial collaboration to critically evaluate theories of consciousness." bioRxiv: 2023.2006.2023.546249.

Dehaene, S., L. Naccache, L. Cohen, D. Le Bihan, J.-F. Mangin, J.-B. Poline and D. Rivière (2001). "Cerebral mechanisms of word masking and unconscious repetition priming." Nature Neuroscience **4**(7): 752-758.

Desikan, R. S., F. Ségonne, B. Fischl, B. T. Quinn, B. C. Dickerson, D. Blacker, R. L. Buckner, A. M. Dale, R. P. Maguire and B. T. Hyman (2006). "An automated labeling system for subdividing the human cerebral cortex on MRI scans into gyral based regions of interest." Neuroimage **31**(3): 968-980.

Ekman, P. and W. V. Friesen (1975). Unmasking the face: A guide to recognizing emotions from facial clues. Oxford, England, Prentice-Hall.

Fischl, B., D. H. Salat, E. Busa, M. Albert, M. Dieterich, C. Haselgrove, A. Van Der Kouwe, R. Killiany, D. Kennedy and S. Klaveness (2002). "Whole brain segmentation: automated labeling of neuroanatomical structures in the human brain." Neuron **33**(3): 341-355.

Glasser, M. F., T. S. Coalson, E. C. Robinson, C. D. Hacker, J. Harwell, E. Yacoub, K. Ugurbil, J. Andersson, C. F. Beckmann, M. Jenkinson, S. M. Smith and D. C. Van Essen (2016). "A multi-modal parcellation of human cerebral cortex." Nature **536**(7615): 171-178.

Huang, C.-C., E. T. Rolls, J. Feng and C.-P. Lin (2022). "An extended Human Connectome Project multimodal parcellation atlas of the human cortex and subcortical areas." Brain Structure and Function **227**(3): 763-778.

Karalis, N., C. Dejean, F. Chaudun, S. Khoder, R. R. Rozeske, H. Wurtz, S. Bagur, K. Benchenane, A. Sirota and J. Courtin (2016). "4-Hz oscillations synchronize prefrontal–amygdala circuits during fear behavior." Nature neuroscience **19**(4): 605-612.

Koch, C., M. Massimini, M. Boly and G. Tononi (2016). "Posterior and anterior cortex — where is the difference that makes the difference?" Nature Reviews Neuroscience **17**(10): 666-666.

Lau, H. (2022). In Consciousness we Trust: The Cognitive Neuroscience of Subjective Experience, Oxford University Press.

Li, F. F., R. VanRullen, C. Koch and P. Perona (2002). "Rapid natural scene categorization in the near absence of attention." Proceedings of the National Academy of Sciences **99**(14): 9596-9601.

Nir, Y., L. Fisch, R. Mukamel, H. Gelbard-Sagiv, A. Arieli, I. Fried and R. Malach (2007). "Coupling between Neuronal Firing Rate, Gamma LFP, and BOLD fMRI Is Related to Interneuronal Correlations." Current Biology **17**(15): 1275-1285.

Nolte, G., O. Bai, L. Wheaton, Z. Mari, S. Vorbach and M. Hallett (2004). "Identifying true brain interaction from EEG data using the imaginary part of coherency." Clinical neurophysiology **115**(10): 2292-2307.

Pelli, D. G. (1997). "The VideoToolbox software for visual psychophysics: Transforming numbers into movies."

Spatial Vision **10**(4): 437-442.
Qin, C., Z. Tan, Y. Pan, Y. Li, L. Wang, L. Ren, W. Zhou and L. Wang (2017). "Automatic and precise localization and cortical labeling of subdural and depth intracranial electrodes." Frontiers in neuroinformatics **11**: 10.
Ray, S., N. Crone, E. Niebur, P. Franaszczuk and S. Hsiao (2008). "Neural Correlates of High-Gamma Oscillations (60-200 Hz) in Macaque Local Field Potentials and Their Potential Implications in Electrocorticography." The Journal of neuroscience : the official journal of the Society for Neuroscience **28**: 11526-11536.
Simonsohn, U. (2018). "Two Lines: A Valid Alternative to the Invalid Testing of U-Shaped Relationships With Quadratic Regressions." Advances in Methods and Practices in Psychological Science **1**(4): 538-555.
Tottenham, N., J. Tanaka, A. Leon, T. McCarry, M. Nurse, T. Hare, D. Marcus, A. Westerlund, B. Casey and C. Nelson (2009). "The NimStim set of Facial Expressions: Judgments from Untrained Research Participants." Psychiatry research **168**: 242-249.
Yeo, B. T., F. M. Krienen, J. Sepulcre, M. R. Sabuncu, D. Lashkari, M. Hollinshead, J. L. Roffman, J. W. Smoller, L. Zöllei and J. R. Polimeni (2011). "The organization of the human cerebral cortex estimated by intrinsic functional connectivity." Journal of neurophysiology.